Cycling Performance and Limitations of LiNiO$_2$ in Solid-State Batteries

Yuan Ma,[a]* Jun Hao Teo,[a] David Kitsche,[a] Thomas Diemant,[b] Florian Strauss,[a] Yanjiao Ma,[c] Damian Goonetilleke,[a] Jürgen Janek,[a,d] Matteo Bianchini[a,e] and Torsten Brezesinski[a]*

[a] *Battery and Electrochemistry Laboratory (BELLA), Institute of Nanotechnology, Karlsruhe Institute of Technology (KIT), Hermann-von-Helmholtz-Platz 1, 76344 Eggenstein-Leopoldshafen, Germany*

[b] *Helmholtz Institute Ulm (HIU), Helmholtzstrasse 11, 89081 Ulm, Germany*

[c] *Institute of Nanotechnology, Karlsruhe Institute of Technology (KIT), Hermann-von-Helmholtz-Platz 1, 76344 Eggenstein-Leopoldshafen, Germany*

[d] *Institute of Physical Chemistry & Center for Materials Science (ZfM/LaMa), Justus-Liebig-University Giessen, Heinrich-Buff-Ring 17, 35392 Giessen, Germany*

[e] *BASF SE, Carl-Bosch-Strasse 38, 67056 Ludwigshafen am Rhein, Germany*

ToC Graphic
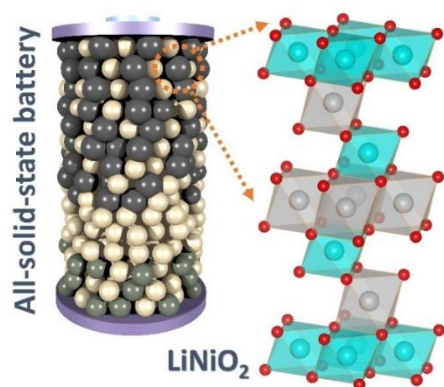
LiNiO$_2$ was tested as a cathode material, for the first time, in a solid-state battery (full cell) environment with argyrodite Li$_6$PS$_5$Cl solid electrolyte. *Operando* and post-mortem investigations show that the performance degradation results predominantly from adverse side reactions at the interfaces during battery operation.

Abstract

Solid-state batteries (SSBs) have been touted as the next major milestone for electrochemical energy storage, improving safety and enabling higher energy densities. $LiNiO_2$ (LNO) has long been considered a promising cathode material, however, its commercial implementation is complicated by stability issues, including reactivity towards the electrolyte components. To address this, a detailed study probing the electrochemical behavior of LNO in pellet-stack SSB cells, in combination with argyrodite Li_6PS_5Cl solid electrolyte (SE) and $Li_4Ti_5O_{12}$ anode, is for the first time presented herein. In this configuration, LNO delivers a specific capacity of 105 mAh/g_{LNO} after 60 cycles (0.2C, 45 °C), which was improved considerably to 153 mAh/g_{LNO} by applying a $LiNbO_3$ coating to the material. Using complementary *operando* and *ex situ* characterization techniques, contributions to the initial capacity loss and capacity fading could be resolved and attributed to decomposition of the argyrodite SE, and volume changes and gas evolution in LNO.

Rechargeable Li-ion batteries (LIBs) employing liquid (organic) electrolytes are a crucial technology enabling energy storage in portable electronics and electric vehicles.[1,2] However, the conventional LIB technology will soon reach its intrinsic specific energy limitation, thus hardly meeting the rapidly increasing demand for safety and higher energy/power densities.[3,4] Because of the liquid electrolyte with its drawbacks of toxicity and flammability, LIBs often suffer from safety concerns. Using a solid electrolyte (SE) instead of a liquid one to build solid-state batteries (SSBs) holds promise for next-generation energy-storage devices.[5,6] Importantly, upon implementation of a Li metal anode, SSBs offer potentially higher energy densities than conventional LIBs.[7] Furthermore, SSBs have other beneficial features, for example, a wide operating temperature range and limited electrode dissolution.[3,5]

An important step towards the development of high-performance SSBs is the fabrication of a cathode composite. Specifically, layered Ni-rich $Li_{1+x}(Ni_{1-y-z}Co_yMn_z)_{1-x}O_2$ (NCM) cathode active materials (CAMs) and lithium thiophosphate SEs are considered a promising combination for application at the cathode side.[8–11] Among thiophosphate SEs, the argyrodite Li_6PS_5Cl is attractive due to its easy processability (softness) and high ionic conductivity (approx. 1.5×10^{-3} S/cm at room temperature).[12,13] Furthermore, within the family of layered oxide CAMs, the endmember composition ($LiNiO_2$, LNO) features both a large theoretical specific capacity (275 mAh/g) and a high mean discharge voltage (3.7 V vs Li^+/Li) while avoiding Co, which is favorable from a cost perspective and to prevent problems related to the current supply chain.[14,15]

To the best of our knowledge, the usage of LNO in SSB cells has yet to be reported, despite its potential for commercial battery applications. As current (commercial) research interests continue to trend towards Co-free and Ni-rich compositions, the study of the endmember LNO, without any cobalt (and/or manganese) contributions, could bring about valuable information on the activity of Ni in these systems, thus driving the research as a whole forward. Herein, we report the behavior of LNO as a CAM in all-inorganic SSBs. By using LNO as a model system and incorporating various

optimization strategies (coating, particle size, etc.), its cycling performance was probed in pelletized cells with Li_6PS_5Cl and $Li_4Ti_5O_{12}$ (LTO) as the SE and anode material, respectively. *Operando* and *ex situ* investigations were carried out to characterize the structural and chemical properties of LNO upon operation, thereby revealing the main limitations of this materials combination.

A summary of the structural and morphological characterization results for the as-prepared LNO CAM is presented in **Figure 1**. The synthesis process is described in the Experimental section (Supporting Information). The powder X-ray diffraction (XRD) pattern and corresponding Rietveld refinement plot (**Figure 1a**) demonstrate that the material has the expected O3-type structure (*R*−3*m* space group), with lattice parameters $a = b = 2.877$ Å and $c = 14.190$ Å and unit cell volume of 101.688 Å^3 (detailed structural parameters are provided in **Table S1**), showing the typical ABCABC stacking of oxygen planes (**Figure 1b**).[16,17] Secondary (impurity) phases were not observed in the XRD pattern. Rietveld analysis further indicates a cation mixing (presence of additional Ni on the Li site, resulting in off-stoichiometry, i.e., $Li_{1-z}Ni_{1+z}O_2$) of $z \approx 2\%$.[14] This was also corroborated by inductively coupled plasma-optical emission spectroscopy (ICP-OES), revealing a slight Ni excess in the material (**Table S1**). The actual material´s stoichiometry was determined to be $[Li_{0.98}Ni_{0.02}]_{3b}[Ni]_{3a}[O_2]_{6c}$ (**Figure 1b**).[14,18] It is well known that the incorporation of a small amount of Ni into the Li layer is almost inevitable due to the similar radii of Li^+ and Ni^{2+}.[14,19,20] However, the cation mixing can be reduced to 1-2% by appropriate synthesis conditions, which is reflected, in our sample, by the fact that the lattice parameters closely match those of well-ordered LNO phases.[16] The overview scanning electron microscopy (SEM) image in **Figure 1c** shows that the particles have a potato-like shape with an average size of 8 μm. As expected, closer examination revealed that the secondary particles consist of 100-300 nm primary particles (**Figure 1d, e**).
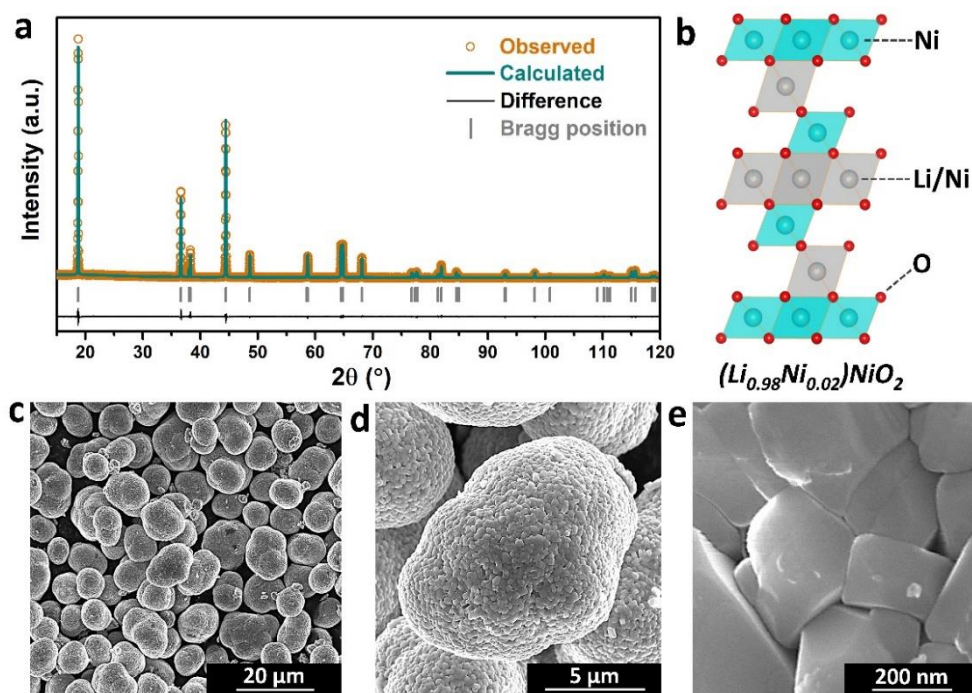
Figure 1. Structural and morphological characteristics of the as-prepared LNO CAM. (a) Powder XRD pattern (Cu-Kα_1) and corresponding Rietveld refinement plot, (b) crystal structure model projected along [110], and (c-e) SEM images at different magnifications.

The electrochemical performance of the as-prepared LNO CAM was probed in pelletized SSBs with Li_6PS_5Cl SE. LNO-based SSB (referred to as LNO-SSB) cells were galvanostatically cycled in the voltage range of 1.35-2.75 V vs $Li_4Ti_5O_{12}/Li_7Ti_5O_{12}$ (corresponding to approx. 2.9-4.3 V vs Li^+/Li) at 45 °C. **Figure 2** shows the cycling stability and Coulombic efficiency of a cell at 0.2C rate over 60 cycles. The first-cycle charge and discharge capacities were 205 and 148 mAh/g_{LNO}, respectively, leading to a low Coulombic efficiency of 72% (**Figure 2a**). As a benchmark, specific charge and discharge capacities of 243 and 228 mAh/g_{LNO}, with a significantly improved Coulombic efficiency of 94%, can be achieved in LNO-based LIB (referred to as LNO-LIB) cells with a Li metal anode cycled under the same conditions. This result already shows that a solid-state environment leads to a reduced Coulombic efficiency in the first cycle,[21] as well as to capacity loss, whose origin will be discussed in more detail below.

Furthermore, an obvious voltage drop of approx. 130 mV was observed in the initial stage of the discharge profile for the LNO-SSB cell (relative to the LNO-LIB cell, see **Figure 2a**), which is indicative of a larger polarization, likely due to surface side reactions increasing the impedance at the CAM/SE interface.[4,22] Interestingly, this overpotential was not apparent during most of the first charge, suggesting that it only originated at a late stage in the delithiation cycle.

The LNO-SSB cell showed about 25% (discharge) capacity loss after 40 cycles, followed by stable cycling until the 60th cycle with 105 mAh/g_{LNO} (**Figure 2b**). The Coulombic efficiency increased to 97 and 98% in the 2nd and 3rd cycle, respectively, and gradually rose with further cycling, eventually stabilizing at 99.9% from the 40th cycle onward. The increase in Coulombic efficiency suggests the formation of a fairly stable passivation layer between the LNO and SE particles, leading to robust cycling after approx. 40 cycles. The LNO-SSB cell also showed a reasonable rate capability (**Figure S1**), which was examined by increasing the C-rate from 0.2 to 1.0C. A reversible specific capacity of 58 mAh/g_{LNO} was achieved at 1.0C, being less than 50% of the initial value at 0.2C rate, thus pointing towards impeded charge transfer across the CAM/SE interface due to the poorly conductive nature of the passivation layer.

In recent years, it has been shown that the particle size is crucial in optimizing the cyclability of layered Ni-rich oxide CAMs in SSBs because of the need for proper ionic and electronic transport.[23–25] In some reports, a smaller CAM particle size improved the contact with the SE and likewise the electronic conductivity of the composite.[23] Here, in an attempt to increase the cycling performance of the LNO CAM, a material with smaller particle size (3 μm on average) was synthesized. However, such an improvement was not observed. Instead, the "small" LNO showed a similar performance to the "large" LNO (**Figure S2**) in otherwise identical cells. This suggests that the low capacity is not due to electronic conductivity limitations, most likely also because of the presence of carbon additive in the composite. Nevertheless, the benefits of using the smaller size CAM became apparent upon application of a protective coating (see below).
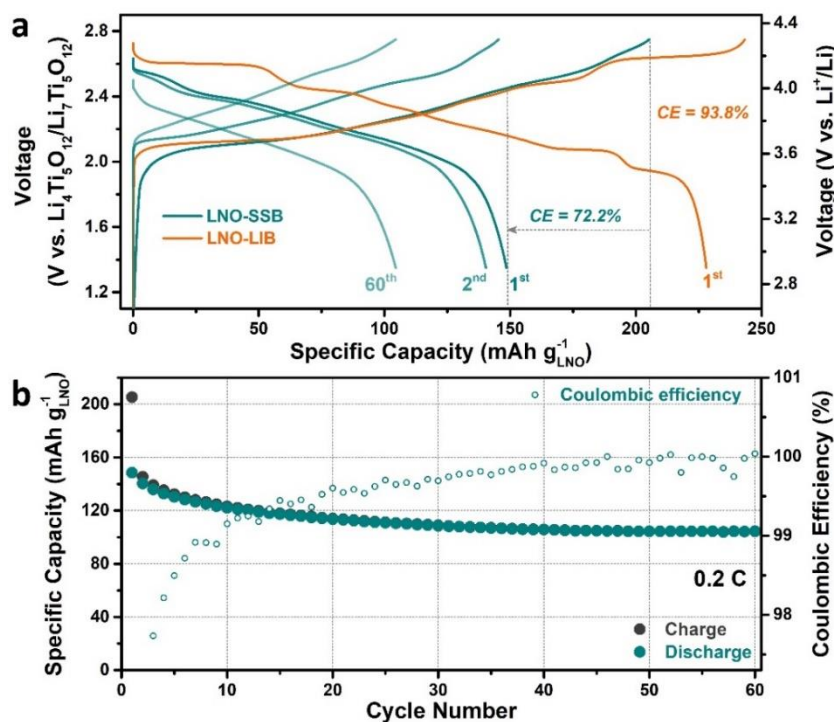
Figure 2. (a) Selected voltage profiles of the LNO-SSB (1st, 2nd, and 60th cycles) and LNO-LIB (1st cycle) cells cycled at a rate of 0.2C and 45 °C. (b) LNO-SSB performance over 60 cycles. Both specific charge and discharge capacities and Coulombic efficiency versus the cycle number are shown.

As discussed above, the major capacity loss occurred in the first cycle. To shed light on the underlying processes, a series of *ex situ* and *operando* measurements were performed.[21] XRD measurements (with LeBail analysis) were conducted on the cathode composite in the pristine state, and also after the initial charging and discharging at 0.2C rate and 45 °C, to determine the state of charge (SOC) and follow the structural evolution of LNO during cycling (**Figure 3**, **Figure S3**, and **Table S2**).[22,23] *Operando* XRD data obtained on a LNO-LIB cell served as reference for the *a* and *c* lattice parameter changes with varying lithium content.[16] **Figure 3a** shows the 003 reflection of LNO with the corresponding plot for the LeBail fit. As expected, the peak shifted to a lower angle upon charging to 2.75 V vs $Li_4Ti_5O_{12}/Li_7Ti_5O_{12}$. Note that no reflections related to the pristine CAM were observable in the XRD pattern in the charged state. This, along with the symmetrical shape of the 003 reflection, confirms

7

the majority (if not all) of the LNO present in the cathode composite to be electrochemically active, owing to the carbon additive improving electronic percolation.[23,26] Upon discharge, the 003 reflection did not shift back to its original position, indicating relatively poor reversibility in the initial cycle. However, it should be noted that also in LNO-LIB cells the CAM never reverts back to the lithiation degree of the pristine state due to significant kinetic hindrance at the end of discharge.[27]

Figure 3b, **c** not only shows the changes in lattice parameters and unit cell volume, but also indicates the different lattice structures adopted by the LNO CAM, namely the hexagonal H1 (in pink), monoclinic M (in blue), hexagonal H2 (in green), and hexagonal H3 (in yellow) phases. After completion of the charging process, an increase of c lattice parameter was observed [$\sin(\vartheta_{003}) = 3/2 \cdot \lambda/c$], which is due to the increase in electrostatic repulsion between the oxygen layers (for low Li content).[16,22,28] In contrast, the a-axis decreased as a result of the Ni oxidation, leading to a contraction of the ab-plane.[16] Note that, although the unit cell volume shrinks overall with delithiation upon charging [$\Delta V/V \approx 2.2\%$ at x(Li) ≈ 0.3], the LNO lattice does not undergo the H2-H3 phase transformation. Hence, the related structural change with collapse of the c-axis is avoided (resulting in significant volume contraction of up to $\Delta V/V = 10\%$).[16,27] This is also evident from the differential capacity plots for the LNO-SSB cells cycled at 0.2 or 0.1C rate in **Figure S4a**.[14,16] While the cell at 0.2C did not show distinct features above 2.6 V vs $Li_4Ti_5O_{12}/Li_7Ti_5O_{12}$, a small peak related to the H2-H3 transition appeared in the dq/dV plot at a rate of 0.1C. However, the x(Li) for the transformation was only approached. When it fully occurs, the related dq/dV peak should have the highest intensity (see LNO-LIB reference data in **Figure S4a**).[16,27] This again confirms the relatively poor charge-transfer kinetics at the CAM/SE interface. Furthermore, when the first two cycles were performed at 0.1C rate and the subsequent cycling at 0.2C, a much faster capacity fading was apparent compared to the cycling done at 0.2C only (**Figure S4b**). One can thus deduce that the H2-H3 phase transformation has a detrimental effect on the long-term cycling performance, most likely due to pronounced mechanical separation between the CAM and SE particles. Clearly, it is

beneficial to avoid the H2-H3 region by maintaining a sufficiently high C-rate (0.2C in the present case) during cycling, although this comes at the expense of lower cell capacities.[29]

The first-cycle specific capacity can be calculated from the Li content, indirectly determined by the refinement analysis.[23] In doing so, a specific charge capacity of 190 mAh/g$_{LNO}$ [$q_{th} \cdot \Delta x$(Li) = $q_{th} \cdot$ (0.99 − 0.30)] was calculated, which is lower than the value from the electrochemical cycling (201 mAh/g$_{LNO}$, **Figure 3c**). The "additional" charge capacity probably stems from the oxidative decomposition of SE.[30,31] The calculated specific discharge capacity of 146 mAh/g$_{LNO}$ [$q_{th} \cdot$ (0.83 − 0.30)] is in good agreement with the electrochemistry results, thereby not only confirming that this approach is viable to determine the SOC of SSBs, but also revealing the SE degradation predominantly taking place upon charging.
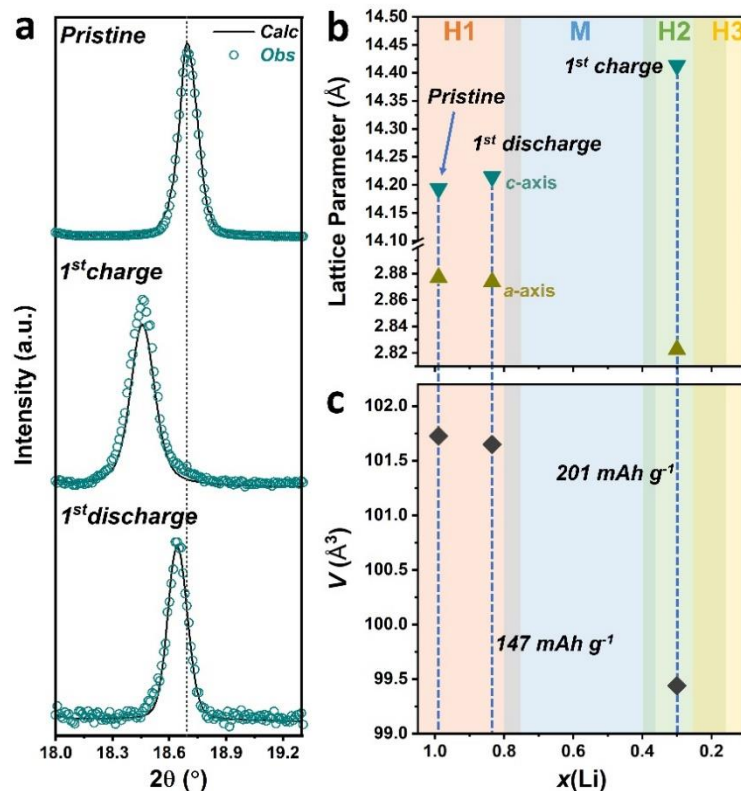
Figure 3. Structural evolution of the LNO CAM in SSB cells cycled at a rate of 0.2C and 45 °C probed by *ex situ* XRD. (a) XRD patterns (Cu-Kα$_1$) in the 2-theta range of the 003 reflection in the pristine, charged, and discharged states with plots for the LeBail fitting.

(b) Refined lattice parameters and (c) unit cell volume. The measured specific charge and discharge capacities are denoted in (c). The x(Li) was determined by comparison of lattice parameters with those derived from *operando* XRD on LNO-LIB cells.[16]

In our previous work, we have demonstrated that LNO-LIB cells suffer from gassing issues during cycling, especially from O_2 evolution and CO_2 evolution within distinct phase regions, contributing to the performance decay.[16] Here, the gassing behavior of the "small" LNO CAM in SSB cells was probed by means of *operando* differential electrochemical mass spectrometry (DEMS, **Figure 4**). The "small" LNO was used for this study to mitigate any potential loss of electrochemical performance resulting from the lower stack pressure applied in the customized setup. The cells for DEMS testing were cycled at 0.05C rate and 45 °C. The use of a low C-rate allowed them to deliver specific charge capacities of $q_{ch} > 210$ mAh/g_{LNO}, thus ensuring sufficient delithiation. Three different gases were detected, H_2, CO_2, and O_2. For SSBs, some H_2 evolution is typically observed in the first charge cycle and could be attributed to the reduction of trace water. In the case of CO_2 evolution in SSB cells, the recorded mass signal ($m/z =$ 44) usually stems from electrochemical decomposition of residual carbonates on the CAM particles. This is generally indicated by the presence of a sharp peak with an onset voltage of $E \geq 4.2$ V vs Li^+/Li and was further confirmed by attenuated total reflection-infrared spectroscopy (ATR-IR) measurements (**Figure S5**).[32] In the present work, however, an additional peak related to CO_2 was observed at the beginning of charge. Such CO_2 evolution in conventional LIBs would be attributed to an electrochemical reduction of the organic carbonate-based electrolyte, which is not applicable to SSBs though.[8] Interestingly, both the CO_2 evolution and the H_2 evolution coincide almost simultaneously at the beginning of the first charge cycle. This suggests that the small amount of initial CO_2 release is associated with the H_2 formation at the anode side (reductive environment).[33]

For Ni-rich NCM CAMs, O_2 evolution has been reported as a consequence of the destabilization of the layered lattice upon delithiation.[34,35] This destabilization at high

SOC also pertains to LNO. In the DEMS experiments, the onset voltage for O_2 evolution during charging was observed at $E \approx 4.2$ V vs Li^+/Li, which is correlated to the H2-H3 phase transformation ($0.26 \geq x(Li) \geq 0.16$ for LNO-LIBs).[16] However, the evolution rate reached a local maximum at the end of the charge cycle (**Figure S6a**), indicating that O_2 evolution primarily results from the intrinsic instability of the H3 phase. Note that O_2 evolution within the H3 phase was observed similarly in LNO-LIBs, albeit in larger amounts.[16] In contrast to LNO-LIBs, no O_2 evolution was detected within the H2 phase region. This could be attributed to the detection limit of the mass spectrometer, as O_2 evolution within the H2 phase was already low for LNO-LIBs. In the first cycle, the total amount of evolved O_2 was approx. 750 nmol/g_{LNO}, which also included gassing at the beginning of discharge (**Figure S6b**, **c**). Overall, it was significantly lower than that of LNO-LIBs.[16] The lower cumulative amount of O_2 evolution could be simply explained by the poorer electrochemical performance (note that it follows an exponential-like relationship with the SOC after reaching the 75% threshold). The higher overpotential resulting from the increased interfacial resistance means that the SSB cell was capable of charging in the main gassing region for a shorter period of time.

The SO_2 mass signal ($m/z = 64$) was also examined. SO_2 evolution has been reported to occur in some sulfide-based SSB cell systems.[8,32] These studies suggest that it stems from the reaction between the SE and highly reactive singlet oxygen (from the CAM lattice and electrochemical carbonate decomposition). In the present work, no SO_2 evolution was detected, which may be due to the relatively low O_2 evolution. Another factor could be the argyrodite SE itself, which was shown to be chemically fairly stable towards oxygen.[32]

Taken together, while both H_2 and CO_2 possibly stem from other components in the SSB setup, the O_2 evolution indeed originates from the irreversible decomposition process of LNO due to stability issues at high degrees of delithiation, causing loss of electroactive material and leading to capacity decay.
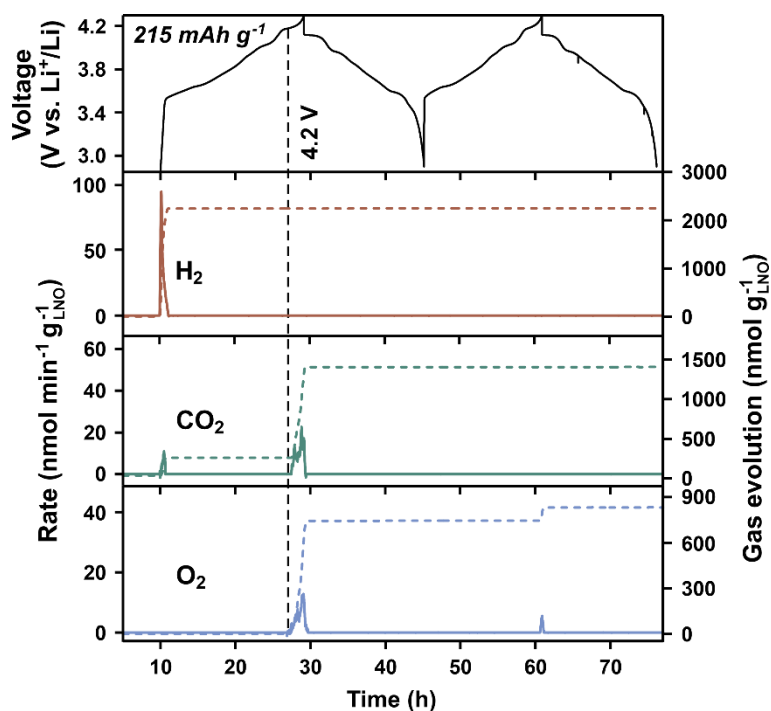
Figure 4. First- and second-cycle voltage profiles of the LNO-SSB cell cycled at a rate of 0.05C and 45 °C with the corresponding time-resolved evolution rates and cumulative amounts for H_2, CO_2, and O_2.

Apart from chemo-mechanical degradation and gassing, performance decay of SSB cells is usually attributed to SE degradation at the interface with the other cell components.[4,36] To gain insight into the chemical nature of the degradation products, *ex situ* X-ray photoelectron spectroscopy (XPS, **Figure 5**) measurements were carried out. **Figure 5a**, **b** shows the S 2p and P 2p core-level spectra for the pristine Li_6PS_5Cl SE, and for the uncycled and cycled composite cathodes. Three doublet peaks can be clearly discerned in the S 2p data of Li_6PS_5Cl. Two of them, at 160.5/161.7 and 161.6/162.8 eV, can be attributed to free S^{2-} ions (or Li_2S impurities) and the PS_4^{3-} units of the argyrodite structure, respectively.[37] The third minor doublet appeared at a higher binding energy (S $2p_{3/2}$ at 162.8 eV) and is probably related to the presence of oxidized sulfur species, such as $P_2S_6^{2-}$.[38] The P 2p spectrum showed the doublet for the PS_4^{3-} units at 131.9/132.7 eV.[37] As expected, it also contained a minor doublet at 133.0/133.7 eV due to the same P_2S_x species mentioned before and/or Li_3PO_4.[37,39,40]

The presence of oxygenated surface impurities in the case of pristine Li_6PS_5Cl is corroborated by the O 1s data shown in **Figure S7**.[39,41] This is primarily because of the high reactivity of the thiophosphate SE towards oxygen and water.[4,12,37] More importantly, the S 2p and P 2p spectra for the as-prepared cathode composite were similar to those of Li_6PS_5Cl. Hence, there were no signs of chemical reactions between the CAM and SE particles during preparation of the cathode pellet. Yet, the signal related to the LNO lattice oxygen was visible at 528.7 eV in the O 1s data.[42] After the initial cycle, the S 2p spectrum showed a new doublet peak at even higher binding energies (S $2p_{3/2}$ at 163.5 eV), indicating SE degradation (formation of polysulfides, etc.).[12,21,38] A new doublet also appeared in the P 2p data (P $2p_{3/2}$ at 134.2 eV) due to the formation of detrimental metal phosphates upon cycling.[37,43] Overall, the degradation leads to the formation of a passivation layer at the CAM/SE interface, resulting in impedance buildup by impeding charge transfer, as can be seen from **Figure 2a**.[8,13] The new doublet peaks increased in intensity after 60 cycles, demonstrating that side reactions continued to occur after the initial cycle (leading to progressive capacity fading), although reduced, in agreement with the gradually increasing Coulombic efficiency discussed above. These findings are also in line with results from electrochemical impedance spectroscopy (EIS) measurements (**Figure S8**), providing direct evidence for the increased resistance $R_{CAM/SE}$. Furthermore, the signal related to the LNO lattice oxygen vanished in the O 1s spectra of the cycled composite cathodes, further confirming the formation of a relatively thick passivation layer, apparently surmounting the XPS information depth.[37]
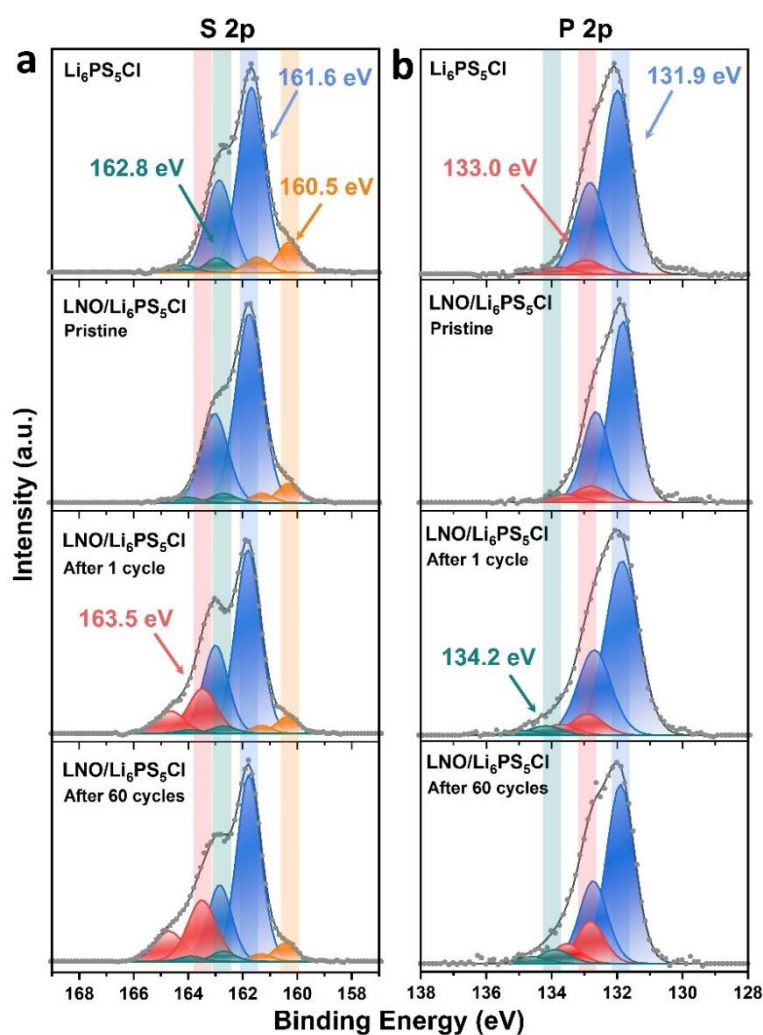
Figure 5. XP detail spectra of the (a) S 2p and (b) P 2p core-level regions for the pristine Li$_6$PS$_5$Cl solid electrolyte and cathode composite in the pristine state, and after 1 and 60 cycles at a rate of 0.2C and 45 °C.

Next, cross-sectional SEM images at different magnifications were taken from the pristine and cycled composite cathodes to visualize the evolution of the interfacial morphology and microstructure (**Figure 6** and **Figure S9**). The SEM image for the pristine pellet (**Figure 6a**) verifies the intimate contact that the LNO secondary particles had with the argyrodite SE. There were no visible voids and cracks or other defects on the micrometer level. However, several minor cracks were apparent near the CAM/SE interface after the initial cycle already, as shown in **Figure 6b**. These cracks increased in length and width with further cycling (**Figure 6c**), indicating progressive

deterioration of the contact between the LNO and SE particles.[21] However, the low-magnification imaging data (**Figure S9**) demonstrate that several of the LNO secondary particles maintained proper contact with the SE. From this data, we conclude that the volume changes of LNO upon (de)lithiation, especially in the initial cycle, lead to some mechanical degradation. Interestingly, under the cycling conditions employed here, the volume change is moderate (approx. 2.2% from the pristine state to the H2 phase), yet already sufficient to induce void formation in the cathode layer, helping to explain the initial capacity loss. In addition, the SEM results demonstrate that the LNO secondary particles maintain their original morphology, without (visible) fracturing occurring. Overall, we can conclude that the causes of the capacity fading are mainly: (i) The partial electrochemical contact loss during cycling and (ii) the formation of a passivation layer between the particles resulting from the interfacial degradation of Li_6PS_5Cl SE.
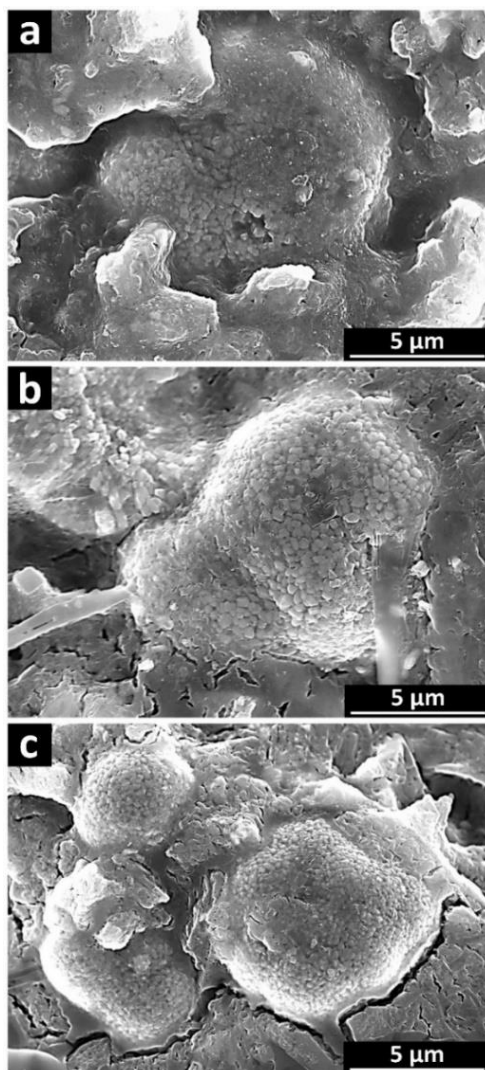
Figure 6. Cross-sectional SEM images of the cathode composite (a) in the pristine state, and after (b) 1 and (c) 60 cycles at a rate of 0.2C and 45 °C.

To isolate and understand the degree of influence these two factors have on the overall capacity fading, a 0.76 wt% LiNbO$_3$ sol-gel coating was applied to the "small" LNO secondary particles (in an attempt to suppress interfacial degradation processes while achieving optimal CAM/SE contact). The successful coating was confirmed by combined SEM/energy-dispersive X-ray spectroscopy (EDS) analysis (**Figure 7a-d** and **Figure S10**). Both the bare and coated "small" LNO CAMs were tested by galvanostatic cycling in SSB cells at 0.2C rate and 45 °C in the same voltage window (1.35-2.75 V vs Li$_4$Ti$_5$O$_{12}$/Li$_7$Ti$_5$O$_{12}$, corresponding to approx. 2.9-4.3 V vs Li$^+$/Li). The beneficial effect

of the LiNbO$_3$ coating on the cycling performance was already evident from the first-cycle voltage profile (**Figure S11a**), revealing substantial improvements in specific discharge capacity (188 vs 148 mAh/g$_{LNO}$) and Coulombic efficiency (87 vs 72%) and emphasizing the competitiveness to previously reported NCM CAMs (**Figure S12** and **Table S3**). *Ex situ* XRD analysis (**Figures S13**-**S15**, and **Tables S4** and **S5**) showed that the LiNbO$_3$-coated LNO undergoes, to some extent, the H2-H3 transition upon delithiation. In contrast, the uncoated material does not, which provides an explanation for the lower specific capacity. However, the larger relative volume changes do not appear to strongly affect the cycling performance. Specifically, the electrochemical testing (**Figure 7e** and **Figure S11b**) revealed that the LiNbO$_3$-coated LNO CAM maintains much better cyclability, delivering specific discharge capacities in excess of 140 mAh/g$_{LNO}$ after 200 cycles (153 mAh/g$_{LNO}$ after 60 cycles), with Coulombic efficiencies close to 100%. These results thus suggest that from the two factors, the formation of a passivation layer plays a more critical role in the capacity fading seen for the LNO-SSB (see also top view and cross-sectional SEM images before/after cycling in **Figure S16**). To alleviate the influence of the H2-H3 phase transformation on this comparison, the SSB using the LiNbO$_3$-coated LNO was also cycled with lower charge cutoff voltages (2.60 and 2.55 V vs Li$_4$Ti$_5$O$_{12}$/Li$_7$Ti$_5$O$_{12}$, corresponding to approx. 4.15 V and 4.10 V vs Li$^+$/Li, respectively). While sacrificing some of the capacity, the respective cells showed a better capacity retention after 200 cycles compared to that cycled in the original voltage window (**Figure S17**). This is due to the absence of the stressful H2-H3 transition during battery operation (**Figure S18**).
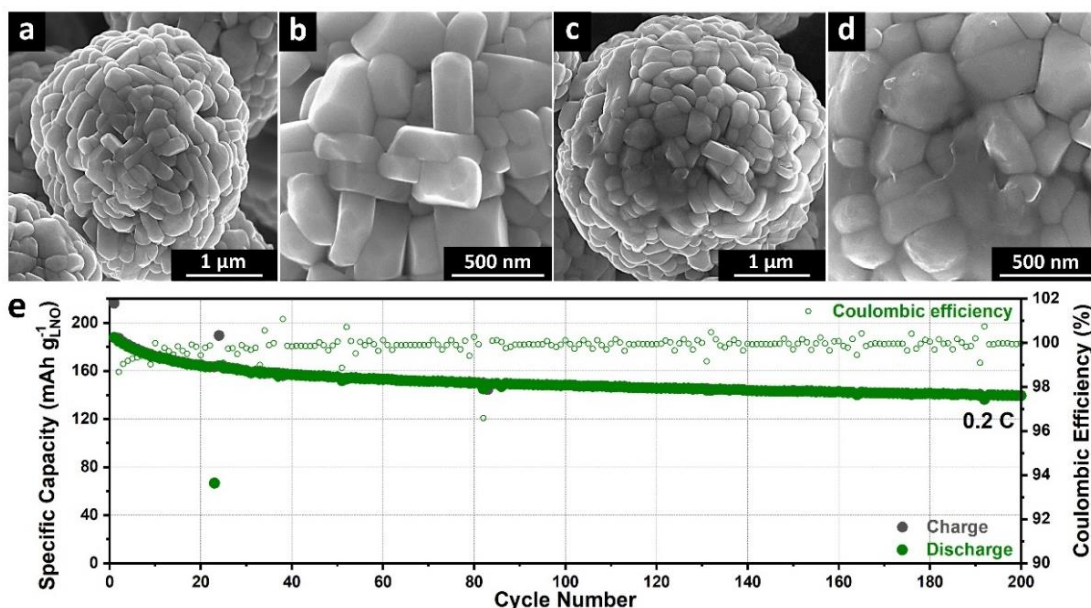
Figure 7. SEM images at different magnifications (a, b) before and (c, d) after coating with sol-gel derived LiNbO$_3$. (e) Long-term cycling performance of the LiNbO$_3$-coated LNO-SSB cell at a rate of 0.2C and 45 °C. Both specific charge and discharge capacities and Coulombic efficiency versus the cycle number are shown.

In the present work, LNO was evaluated, for the first time, as a potential CAM for usage in Li$_6$PS$_5$Cl-based SSB cells, and as a model system for the application of layered Ni-rich oxides approaching the endmember composition. The LNO-SSB exhibited acceptable cycling characteristics, especially when considering that no protective coating was applied to the CAM. Specifically, the bare material delivered a specific discharge capacity of 105 mAh/g$_{LNO}$ at 0.2C rate and 45 °C after 60 cycles and showed a reasonable rate performance (approx. 60 mAh/g$_{LNO}$ at 1.0C). However, compared to liquid electrolyte-based LIB cells, the LNO CAM in the solid-state environment displayed a much lower first-cycle Coulombic efficiency (reversibility). Based on XRD, DEMS, XPS, EIS, and electron microscopy results, we showed that the capacity loss is due to multiple issues: (i) Mechanical degradation resulting from the volume changes of LNO during cycling, (ii) outgassing (especially lattice oxygen loss at high SOC) introducing irreversible changes to the material properties, and (iii) SE degradation and accompanied buildup of passivation byproducts at the CAM/SE interface. These

findings emphasize the critical relevance of unwanted side reactions, gassing, and chemo-mechanical processes in SSBs. The formation of a passivation layer was shown to be the dominant cause of performance decay. Nevertheless, by surface coating of the CAM with a $LiNbO_3$ protective layer, we were able to significantly improve the cell cyclability. This study demonstrates that LNO holds great potential for SSB applications and further modifications to the surface chemistry and/or cycling protocol are key to improving its cycling performance and stability. These findings are also of general relevance for other layered Ni-rich oxide systems and can potentially guide future research into their application in SSB cells.

Associated Content

Supporting Information

Experimental section; structural parameters from Rietveld analyses; rate performance and long-term cycling data; *ex situ* XRD patterns and LeBail fitting results; differential capacity plots; ATR-IR data; additional DEMS results; O 1s XP spectra; Nyquist plots of the electrochemical impedance; SEM imaging and elemental mapping; voltage profiles; performance characteristics of NCM and LNO composite cathodes.

Author Information

Corresponding Authors

*Phone: +49 721 60828051; Email: yuan.ma@kit.edu

*Phone: +49 721 60828827; Email: torsten.brezesinski@kit.edu

Notes

The authors declare no competing financial interest.

Acknowledgements

References

(1) Bresser, D.; Passerini, S.; Scrosati, B. Leveraging Valuable Synergies by Combining Alloying and Conversion for Lithium-Ion Anodes. *Energy Environ. Sci.* **2016**, *9*, 3348–3367.

(2) Ma, Y.; Ma, Y.; Kim, G.; Diemant, T.; Behm, R. J.; Geiger, D.; Kaiser, U.; Varzi, A.; Passerini, S. Superior Lithium Storage Capacity of α-MnS Nanoparticles Embedded in S-Doped Carbonaceous Mesoporous Frameworks. *Adv. Energy Mater.* **2019**, *9*, 1902077.

(3) Janek, J.; Zeier, W. G. A Solid Future for Battery Development. *Nat. Energy* **2016**, *1*, 16141.

(4) Banerjee, A.; Wang, X.; Fang, C.; Wu, E. A.; Meng, Y. S. Interfaces and Interphases in All-Solid-State Batteries with Inorganic Solid Electrolytes. *Chem. Rev.* **2020**, *120*, 6878–6933.

(5) Lee, J.; Lee, K.; Lee, T.; Kim, H.; Kim, K.; Cho, W.; Coskun, A.; Char, K.; Choi, J. W. In Situ Deprotection of Polymeric Binders for Solution-Processible Sulfide-Based All-Solid-State Batteries. *Adv. Mater.* **2020**, *32*, 2001702.

(6) Marinaro, M.; Bresser, D.; Beyer, E.; Faguy, P.; Hosoi, K.; Li, H.; Sakovica, J.; Amine, K.; Wohlfahrt-Mehrens, M.; Passerini, S. Bringing Forward the Development of Battery Cells for Automotive Applications: Perspective of R&D Activities in China, Japan, the EU and the USA. *J. Power Sources* **2020**, *459*, 228073.

(7)   Randau, S.; Weber, D. A.; Kötz, O.; Koerver, R.; Braun, P.; Weber, A.; Ivers-Tiffée, E.; Adermann, T.; Kulisch, J.; Zeier, W. G.; Richter, F. H.; Janek, J. Benchmarking the Performance of All-Solid-State Lithium Batteries. *Nat. Energy* **2020**, *5*, 259–270.

(8)   Kim, A.-Y.; Strauss, F.; Bartsch, T.; Teo, J. H.; Hatsukade, T.; Mazilkin, A.; Janek, J.; Hartmann, P.; Brezesinski, T. Stabilizing Effect of a Hybrid Surface Coating on a Ni-Rich NCM Cathode Material in All-Solid-State Batteries. *Chem. Mater.* **2019**, *31*, 9664–9672.

(9)   Deng, S.; Sun, Q.; Li, M.; Adair, K.; Yu, C.; Li, J.; Li, W.; Fu, J.; Li, X.; Li, R.; Hu, Y.; Chen, N.; Huang, H.; Zhang, L.; Zhao, S.; Lu, S.; Sun, X. Insight into Cathode Surface to Boost the Performance of Solid-State Batteries. *Energy Storage Mater.* **2021**, *35*, 661–668.

(10)   Liu, X.; Zheng, B.; Zhao, J.; Zhao, W.; Liang, Z.; Su, Y.; Xie, C.; Zhou, K.; Xiang, Y.; Zhu, J.; Wang, H.; Zhong, G.; Gong, Z.; Huang, J.; Yang, Y. Electrochemo-Mechanical Effects on Structural Integrity of Ni-Rich Cathodes with Different Microstructures in All Solid-State Batteries. *Adv. Energy Mater.* **2021**, *11*, 2003583.

(11)   Jung, S. H.; Kim, U.; Kim, J.; Jun, S.; Yoon, C. S.; Jung, Y. S.; Sun, Y. Ni-Rich Layered Cathode Materials with Electrochemo-Mechanically Compliant Microstructures for All-Solid-State Li Batteries. *Adv. Energy Mater.* **2020**, *10*, 1903360.

(12)   Zhang, J.; Zheng, C.; Li, L.; Xia, Y.; Huang, H.; Gan, Y.; Liang, C.; He, X.; Tao, X.; Zhang, W. Unraveling the Intra and Intercycle Interfacial Evolution of Li_6PS_5Cl-Based All-Solid-State Lithium Batteries. *Adv. Energy Mater.* **2020**, *10*, 1903311.

(13)   Culver, S. P.; Koerver, R.; Zeier, W. G.; Janek, J. On the Functionality of Coatings for Cathode Active Materials in Thiophosphate-Based All-Solid-State Batteries. *Adv. Energy Mater.* **2019**, *9*, 1900626.

(14)   Bianchini, M.; Roca-Ayats, M.; Hartmann, P.; Brezesinski, T.; Janek, J. There and Back Again—The Journey of $LiNiO_2$ as a Cathode Active Material. *Angew. Chem.*

Int. Ed. **2019**, *58*, 10434–10458.

(15) Nitta, N.; Wu, F.; Lee, J. T.; Yushin, G. Li-Ion Battery Materials: Present and Future. *Mater. Today* **2015**, *18*, 252–264.

(16) de Biasi, L.; Schiele, A.; Roca-Ayats, M.; Garcia, G.; Brezesinski, T.; Hartmann, P.; Janek, J. Phase Transformation Behavior and Stability of LiNiO$_2$ Cathode Material for Li-Ion Batteries Obtained from In Situ Gas Analysis and Operando X-Ray Diffraction. *ChemSusChem* **2019**, *12*, 2240–2250.

(17) Delmas, C.; Fouassier, C.; Hagenmuller, P. Structural Classification and Properties of the Layered Oxides. *Phys. B+C* **1980**, *99*, 81–85.

(18) Kanno, R.; Kubo, H.; Kawamoto, Y.; Kamiyama, T.; Izumi, F.; Takeda, Y.; Takano, M. Phase Relationship and Lithium Deintercalation in Lithium Nickel Oxides. *J. Solid State Chem.* **1994**, *110*, 216–225.

(19) Delmas, C.; Ménétrier, M.; Croguennec, L.; Saadoune, I.; Rougier, A.; Pouillerie, C.; Prado, G.; Grüne, M.; Fournès, L. An Overview of the Li(Ni,M)O$_2$ Systems: Syntheses, Structures and Properties. *Electrochim. Acta* **1999**, *45*, 243–253.

(20) Delmas, C.; Pérès, J. P.; Rougier, A.; Demourgues, A.; Weill, F.; Chadwick, A.; Broussely, M.; Perton, F.; Biensan, P..; Willmann, P. On the Behavior of the Li$_x$NiO$_2$ System: An Electrochemical and Structural Overview. *J. Power Sources* **1997**, *68*, 120–125.

(21) Koerver, R.; Aygün, I.; Leichtweiß, T.; Dietrich, C.; Zhang, W.; Binder, J. O.; Hartmann, P.; Zeier, W. G.; Janek, J. Capacity Fade in Solid-State Batteries: Interphase Formation and Chemomechanical Processes in Nickel-Rich Layered Oxide Cathodes and Lithium Thiophosphate Solid Electrolytes. *Chem. Mater.* **2017**, *29*, 5574–5582.

(22) Bartsch, T.; Kim, A.-Y.; Strauss, F.; de Biasi, L.; Teo, J. H.; Janek, J.; Hartmann, P.; Brezesinski, T. Indirect State-of-Charge Determination of All-Solid-State Battery Cells by X-Ray Diffraction. *Chem. Commun.* **2019**, *55*, 11223–11226.

(23) Strauss, F.; Bartsch, T.; de Biasi, L.; Kim, A.-Y.; Janek, J.; Hartmann, P.; Brezesinski, T. Impact of Cathode Material Particle Size on the Capacity of Bulk-Type All-Solid-State Batteries. *ACS Energy Lett.* **2018**, *3*, 992–996.

(24) Kim, B.-C.; Takada, K.; Ohta, N.; Seino, Y.; Zhang, L.; Wada, H.; Sasaki, T. All Solid State Li-Ion Secondary Battery with FeS Anode. *Solid State Ion.* **2005**, *176*, 2383–2387.

(25) Peng, G.; Yao, X.; Wan, H.; Huang, B.; Yin, J.; Ding, F.; Xu, X. Insights on the Fundamental Lithium Storage Behavior of All-Solid-State Lithium Batteries Containing the $LiNi_{0.8}Co_{0.15}Al_{0.05}O_2$ Cathode and Sulfide Electrolyte. *J. Power Sources* **2016**, *307*, 724–730.

(26) Strauss, F.; Stepien, D.; Maibach, J.; Pfaffmann, L.; Indris, S.; Hartmann, P.; Brezesinski, T. Influence of Electronically Conductive Additives on the Cycling Performance of Argyrodite-Based All-Solid-State Batteries. *RSC Adv.* **2020**, *10*, 1114–1119.

(27) Li, H.; Zhang, N.; Li, J.; Dahn, J. R. Updating the Structure and Electrochemistry of Li_xNiO_2 for $0 \leq x \leq 1$. *J. Electrochem. Soc.* **2018**, *165*, A2985–A2993.

(28) Van der Ven, A.; Aydinol, M. K.; Ceder, G.; Kresse, G.; Hafner, J. First-Principles Investigation of Phase Stability in Li_xCoO_2. *Phys. Rev. B* **1998**, *58*, 2975–2987.

(29) Yoon, C. S.; Jun, D.-W.; Myung, S.-T.; Sun, Y.-K. Structural Stability of $LiNiO_2$ Cycled above 4.2 V. *ACS Energy Lett.* **2017**, *2*, 1150–1155.

(30) Walther, F.; Randau, S.; Schneider, Y.; Sann, J.; Rohnke, M.; Richter, F. H.; Zeier, W. G.; Janek, J. Influence of Carbon Additives on the Decomposition Pathways in Cathodes of Lithium Thiophosphate-Based All-Solid-State Batteries. *Chem. Mater.* **2020**, *32*, 6123–6136.

(31) Koerver, R.; Walther, F.; Aygün, I.; Sann, J.; Dietrich, C.; Zeier, W. G.; Janek, J. Redox-Active Cathode Interphases in Solid-State Batteries. *J. Mater. Chem. A* **2017**, *5*, 22750–22760.

(32) Strauss, F.; Teo, J. H.; Schiele, A.; Bartsch, T.; Hatsukade, T.; Hartmann, P.; Janek, J.; Brezesinski, T. Gas Evolution in Lithium-Ion Batteries: Solid versus Liquid Electrolyte. *ACS Appl. Mater. Interfaces* **2020**, *12*, 20462–20468.

(33) Lux, S.; Baldauf-Sommerbauer, G.; Siebenhofer, M. Hydrogenation of Inorganic Metal Carbonates: A Review on Its Potential for Carbon Dioxide Utilization and Emission Reduction. *ChemSusChem* **2018**, *11*, 3357–3375.

(34) Jung, R.; Metzger, M.; Maglia, F.; Stinner, C.; Gasteiger, H. A. Chemical versus Electrochemical Electrolyte Oxidation on NMC111, NMC622, NMC811, LNMO, and Conductive Carbon. *J. Phys. Chem. Lett.* **2017**, *8*, 4820–4825.

(35) Jung, R.; Strobl, P.; Maglia, F.; Stinner, C.; Gasteiger, H. A. Temperature Dependence of Oxygen Release from $LiNi_{0.6}Mn_{0.2}Co_{0.2}O_2$ (NMC622) Cathode Materials for Li-Ion Batteries. *J. Electrochem. Soc.* **2018**, *165*, A2869–A2879.

(36) Park, J.; Kim, K. T.; Oh, D. Y.; Jin, D.; Kim, D.; Jung, Y. S.; Lee, Y. M. Digital Twin-Driven All-Solid-State Battery: Unraveling the Physical and Electrochemical Behaviors. *Adv. Energy Mater.* **2020**, *10*, 2001563.

(37) Walther, F.; Koerver, R.; Fuchs, T.; Ohno, S.; Sann, J.; Rohnke, M.; Zeier, W. G.; Janek, J. Visualization of the Interfacial Decomposition of Composite Cathodes in Argyrodite Based All-Solid-State Batteries Using Time-of-Flight Secondary Ion Mass Spectrometry. *Chem. Mater.* **2019**, *31*, 3745-3755.

(38) Park, S. W.; Oh, G.; Park, J.; Ha, Y.; Lee, S.; Yoon, S. Y.; Kim, B. G. Graphitic Hollow Nanocarbon as a Promising Conducting Agent for Solid-State Lithium Batteries. *Small* **2019**, *15*, 1900235.

(39) Appapillai, A. T.; Mansour, A. N.; Cho, J.; Shao-Horn, Y. Microstructure of $LiCoO_2$ with and without "$AlPO_4$" Nanoparticle Coating: Combined STEM and XPS Studies. *Chem. Mater.* **2007**, *19*, 5748–5757.

(40) Wang, B.; Liu, J.; Sun, Q.; Li, R.; Sham, T.-K.; Sun, X. Atomic Layer Deposition of Lithium Phosphates as Solid-State Electrolytes for All-Solid-State Microbatteries.

Nanotechnology **2014**, *25*, 504007.

(41)   Nagao, K.; Hayashi, A.; Deguchi, M.; Tsukasaki, H.; Mori, S.; Tatsumisago, M. Amorphous $LiCoO_2$–Li_2SO_4 Active Materials: Potential Positive Electrodes for Bulk-Type All-Oxide Solid-State Lithium Batteries with High Energy Density. *J. Power Sources* **2017**, *348*, 1–8.

(42)   Moses, A. W.; Flores, H. G. G.; Kim, J.-G.; Langell, M. A. Surface Properties of $LiCoO_2$, $LiNiO_2$ and $LiNi_{1-x}Co_xO_2$. *Appl. Surf. Sci.* **2007**, *253*, 4782–4791.

(43)   Franke, R.; Chassé, Th.; Streubel, P.; Meisel, A. Auger Parameters and Relaxation Energies of Phosphorus in Solid Compounds. *J. Electron Spectrosc. Relat. Phenom.* **1991**, *56*, 381–388.